

# Measurement of the Sunyaev-Zel'dovich effect around cosmic voids

David Alonso<sup>1,\*</sup>, J. Colin Hill<sup>2</sup>, Renee Hlozek<sup>3</sup>, and David N. Spergel<sup>4,5</sup>

<sup>1</sup>*University of Oxford, Denys Wilkinson Building, Keble Road, Oxford OX1 3RH, UK*

<sup>2</sup>*Department of Astronomy, Columbia University, New York, NY 10027, USA*

<sup>3</sup>*Dunlap Institute for Astronomy and Astrophysics, University of Toronto*

<sup>4</sup>*Center for Computational Astrophysics, Flatiron Institute,  
162 5th Avenue, 10010, New York, NY, USA and*

<sup>5</sup>*Department of Astrophysical Sciences, Princeton University, Peyton Hall, Princeton NJ 08544-0010, USA*

We stack maps of the thermal Sunyaev-Zel'dovich effect produced by the Planck collaboration around the centers of cosmic voids defined by the distribution of galaxies in the CMASS sample of the Baryon Oscillation Spectroscopic Survey, scaled by the void effective radii. We report a first detection of the associated cross-correlation at the  $\sim 3.4\sigma$  level. We compare the measured excess Compton- $y$  profile around voids with a model based solely on the spatial modulation of halo abundance with environmental density. Scaling this expected profile by an overall amplitude  $\alpha_v$ , we find a best-fit value  $\alpha_v = 0.67 \pm 0.2$ . We discuss the possible interpretations of this measurement in terms of modelling uncertainties, excess pressure in low-mass halos or non-local heating mechanisms.

## I. INTRODUCTION

**DA: Introduction: how cool and useful voids are. What the SZ effect is and current cool things that have been done with it. The interest of measuring the temperature of different environments...**

Throughout this paper we assumed a flat  $\Lambda$ CDM cosmology with parameters  $\Omega_M = 0.3$ ,  $h = 0.7$ ,  $\sigma_8 = 0.8$ ,  $n_s = 0.96$ , where  $\Omega_M$  is the fractional density of non-relativistic species today,  $h$  is the normalized expansion rate,  $\sigma_8$  is the standard deviation of the linear matter overdensity in spheres with a radius of  $8 h^{-1} \text{Mpc}$  and  $n_s$  is the primordial spectral index of scalar perturbations. The choice of  $\Omega_M$  was made to coincide with the value assumed in the construction of the void catalog used in this analysis (see Section REF). This was necessary in order to transform the comoving lengths used in the catalog into projected angular separations.

## II. THE EXPECTED VOID SZ PROFILE

The thermal Sunyaev-Zel'dovich effect [1] traces the hot gas in the Universe through the inverse Compton scattering of CMB photons by high-energy electrons. This induces a spatial and spectral distortion in the CMB given by

$$\frac{\Delta T}{T_{\text{CMB}}} = g \left( \frac{h\nu}{kT_{\text{CMB}}} \right) y(\hat{\mathbf{n}}), \quad (1)$$

where  $g(x) = x \coth(x/2) - 4$ ,  $y$  is the so-called Compton- $y$  parameter (see below) and we have neglected all relativistic corrections.

The Compton- $y$  parameter associated to a particular structure at redshift  $z$  is given by

$$y(\theta) = \frac{\sigma_T}{m_e c^2} \int \frac{dr_{\parallel}}{1+z} P_e \left( \sqrt{r_{\parallel}^2 + r_{\perp}^2} \right), \quad (2)$$

where  $\sigma_T$  and  $m_e$  are the Thomson scattering cross section and the electron mass,  $P_e(r)$  is the electron pressure profile of the structure,  $r_{\parallel}$  and  $r_{\perp} \equiv \chi(z)\theta$  are the longitudinal (parallel to the line of sight) and transverse comoving distances from the structure,  $\chi(z)$  is the comoving distance to redshift  $z$  and  $\theta$  is the angular separation from the center of the projected structure.

The tSZ signal around voids can therefore be predicted by estimating their expected excess electron pressure profile. This is directly connected to the problem of modelling the mechanisms by which baryons are heated in different environments, which has been approached from different angles in the literature. One approach is to assume that heating processes take place mostly in the dense environments of dark matter halos, and that the gas density and temperature can be related to halo mass (e.g. [2] **DA: add other relevant references?**). Under this assumption, the void pressure profile can be directly computed in terms of the abundance of haloes of different masses conditional to the environmental density given a model for the relation between halo mass and gas density and pressure. Such a “local” heating mechanism would predict voids to be colder than the average, given the under-abundance of massive, hotter halos in underdense environments [3]. This description neglects other non-local sources of heating of the inter-galactic medium, such as the effect of TeV blazars in the presence of plasma instabilities [4], which could even give rise to an inverted density-temperature relation [5] **DA: not sure if we should be citing other models.**

We do so here by connecting the void density profile, which can be estimated directly from the data, with  $P_e(r)$  using the so-called “effective universe” approach. This method is spelled out in Appendix A, and has been previously used in analyses of environmental effects on halo

---

\* david.alonso@physics.ox.ac.uk

abundances [6–9]). In short, one can associate the void underdensity  $\delta(r)$  with a set of effective cosmological parameters  $\Omega_X(r)$ , which can then be used to estimate any quantity in the void as its background value in that effective cosmology.

The problem therefore reduces to estimating the background free electron pressure for a given set of cosmological parameters. Assuming the main contribution to the total tSZ signal comes from the hot gas in dark matter haloes, the total electron pressure at a point  $\mathbf{r}$  is given by the sum of the contributions from all haloes:

$$P_e(\mathbf{r}) = \int d\mathbf{x}^3 dM n(M, \mathbf{x}) P_e(|\mathbf{x} - \mathbf{r}|, M), \quad (3)$$

where  $n(M, \mathbf{x})$  is the number density of haloes of mass  $M$  (i.e. the position-dependent halo mass function), with pressure profile  $P_e(r, M)$ . The background contribution to the electron pressure is therefore found by taking the ensemble average of the equation above:

$$\langle P_e \rangle = \int dM n(M) \frac{4\pi}{3} \int dr r^2 P_e(r, M). \quad (4)$$

To summarize, the process to estimate the void’s electron pressure profile is therefore as follows:

1. Estimate the void’s over-density profile  $\delta(r)$ .
2. At a given  $r$ , relate  $\delta(r)$  to a set of effective cosmological parameters  $\Omega_X(r)$  as described in Appendix A.
3. The void’s electron pressure at that  $r$  is then computed using Eq. 4 as the background electron pressure for the corresponding effective cosmology parameters. Note that, in this equation, both the mass function and the halo pressure profile depend on  $\Omega_X$ .
4. Integrate the void pressure profile along the line of sight (Eq. 2) to obtain the expected tSZ signal.

Here we used the estimate of the halo mass function by [10], and the electron pressure profile of [11]. The void density profile  $\delta(r)$  was estimated directly from the data in terms of the galaxy overdensity (see Section IV A). We computed the fiducial  $y$  profile used here at a fixed redshift  $z = 0.5$ , corresponding to the median redshift of the CMASS sample, and we verified that the resulting curve does not vary significantly with  $z$  within the allowed redshift range. Note that, since all our results are given in terms of the ratio  $\theta/\theta_s$ , where  $\theta$  is the angular distance to the void centre and  $\theta_v$  is the projected void radius, redshift-dependent projection effects are negligible.

### III. DATA

#### A. Void catalogs

We use the public void catalog described in [12], constructed using the ZOBOV void finding algorithm

[13], which connects underdensities identified through a Voronoi tessellation using a “watershed” method. The catalog is based on the 12th Data Release of the Baryon Oscillation Spectroscopic Survey (BOSS) [14], part of the Sloan Digital Sky Survey. The full BOSS catalog, covering roughly  $10,000 \text{ deg}^2$ , is sub-divided into two galaxy samples spanning complementary redshift ranges, LOWZ ( $\sim 4.6 \times 10^5$  objects,  $0.2 < z < 0.43$ ) and CMASS ( $\sim 8.5 \times 10^5$  objects,  $0.43 < z < 0.7$ ), and void catalogs are provided for both samples<sup>1</sup>. Although the authors identified more than 10,000 voids in the BOSS dataset, we focused our analysis only on the “cut” version of the catalogs, in which cuts on significance and minimum density were made to ensure a clean sample of underdense regions. In particular we use the CMASS-based catalog, containing 774 voids. Each void is assigned an effective radius  $r_v$  corresponding to the radius of the sphere encompassing its Voronoi volume.

For this sample the authors also provide 1,000 mock realizations generated from a set of simplified N-body simulations. These mocks are based on a galaxy sample that reproduces the clustering properties of the CMASS sample, as well as its angular completeness and redshift distribution. As reported by [12], the resulting void mock catalogs contain on average  $\sim 20\%$  more voids than the true data, although they reproduce statistics of the true void data well in terms of angular, redshift and size distribution. We therefore randomly downsampled the mocks to correct for this issue. These mocks were used both as randoms to compute the stacked signal around the true voids and as ensemble realizations to estimate the measurement uncertainties.

Besides the void catalogs we also made use of the full CMASS galaxy sample, as well as the corresponding random catalogues made available by the BOSS collaboration, to estimate the average void density profile<sup>2</sup>.

#### B. tSZ and CMB maps

In order to estimate the Sunyaev-Zel’dovich signal associated with voids we make use of the Compton- $y$  parameter maps made available by the Planck collaboration [15]. The available maps were derived as linear combinations of the Planck High-Frequency Instrument (HFI) intensity maps (100 GHz, 143 GHz, 217 GHz, 353 GHz, 545 GHz and 857 GHz) smoothed to a common resolution of  $\theta_{\text{FWHM}} = 10 \text{ arcmin}$ . The Planck collaboration has released two  $y$  maps derived using different reconstruction methods: the Modified Internal Linear Combination Algorithm (MILCA, [16]) and the Needlet Internal Linear Combination (NILC, [17]). In both cases, the separation

<sup>1</sup> The void catalogs used here are available at <http://lss.phy.vanderbilt.edu/voids/>.

<sup>2</sup> The CMASS data is available at <https://data.sdss.org/sas/dr12/boos/lss/>

of the tSZ signal from other sources of emission (CMB and foregrounds) is based mainly on its well-known frequency dependence, and both methods find linear combinations of the multi-frequency maps that minimize the variance of the resulting map while preserving a unit response to the SZ frequency dependence and de-projecting the CMB. The methods also use spatial information by constructing independent weights for different scales, although they differ in the details of how these weights are derived (see [15]).

There are hints that the NILC is less reliable for the kind of measurement we want to make (e.g. [18]), possibly due to its large-scale noise power [15], which could be difficult to subtract in the absence of highly accurate random catalogs. This is especially true in the case of stacking on voids subtending relatively large angular scales. For this reason we base our analysis on the MILCA  $y$  map, although we studied the consistency of our results using the NILC map (see Section IV C).

In order to mitigate the contamination from galactic and extragalactic foregrounds we use a combination of the Planck 60% galactic mask and the union of the HFI and LFI point-source masks. In an effort to enhance the signal-to-noise ratio ( $S/N$ ) in our measurement, we further mask all SZ sources detected by Planck [19] above  $5\sigma$  with redshifts  $z < 0.43$  (i.e. uncorrelated with the CMASS voids). We also make use of the HFI 545 GHz map [20] to constrain the level of foreground and CIB contamination (see Section IV C)<sup>3</sup>.

## IV. RESULTS

### A. The void density profile

Our prediction for the expected void  $y$  profile (Section II) requires an estimate of the average density profile. The void density profile  $\delta(r)$  has been the subject of much study in recent years [21–23], and has been shown to take a fairly universal shape across size, redshift and, more importantly, tracer of the underlying density field [24, 25].

We estimate the void underdensity from the density of tracer galaxies in the CMASS sample, using the corresponding random catalog to correct for edge effects and incompleteness. For each void  $i$  we compute the number of data and random objects found in bins of  $x = r/r_v^i$ , where  $r$  is comoving distance from the object to the centre of the void and  $r_v^i$  is the void’s effective radius. The average density profile is then estimated as:

$$1 + \delta_g(x) = \frac{N_R \sum_i D_i(x = r/r_v^i)}{N_D \sum_i R_i(x = r/r_v^i)}, \quad (5)$$

where  $D_i$  and  $R_i$  are the histograms of data and random objects found around the  $i$ -th void,  $N_D$  and  $N_R$  are the total size of the data and random catalogs respectively and the index  $i$  runs across all the voids in the catalog.

The density profile thus computed corresponds to the underdensity of tracer CMASS galaxies around these voids at the median redshift  $z \sim 0.5$ . The effective-universe approach, as described in Appendix A, is formulated in terms of the matter underdensity at redshift  $z = 0$ . To compute this latter quantity in terms of  $\delta_g(x|z = 0.5)$  we must therefore account for the effects of galaxy bias and structure growth. To do so we simply rescale  $\delta_g$  by a factor  $[b_{\text{CMASS}} D(z = 0.5)]^{-1}$ , where  $b_{\text{CMASS}} = 2.0$  is the bias of the CMASS sample [26] and  $D(z)$  is the linear growth factor normalized at  $z = 0$ . Note that, although in general non-linear contributions to both growth and galaxy biasing become important on small scales, recent studies find that this problem is alleviated around voids [27, 28], and this simple linear rescaling should be a good approximation given the uncertainties reported here.

### B. The SZ signal around voids

In order to estimate the average tSZ signal around cosmic voids we proceed as follows:

1. For each void  $i$  in the catalog, at redshift  $z_i$  and with effective radius  $r_v^i$ , we loop over all pixels in the  $y$  map lying within a radius  $3\theta_v^i$  of the void’s centre, where  $\theta_v^i = r_v^i/\chi(z_i)$  is the angle subtended by the void’s effective radius (here  $\chi(z)$  is the comoving distance to redshift  $z$ ). For each pixel  $p$  we compute two quantities:  $x_p \equiv \theta_{i,p}/\theta_v^i$  and  $\psi_p$ , where  $\theta_{i,p}$  is the angular separation between the pixel and void centres, and  $\psi_{i,p}$  is the angle that this separation vector forms with the great circle connecting the pixel with the North Pole.
2. For each void we then produce two 2-dimensional histograms,  $s_y^i(x, \psi)$  and  $s_N^i(x, \psi)$

$$s_y^i(x, \psi) = \sum_p \Theta(\psi_p, \psi, \Delta\psi) \Theta(x_p, x, \Delta x) y_p$$

$$s_N^i(x, \psi) = \sum_p \Theta(\psi_p, \psi, \Delta\psi) \Theta(x_p, x, \Delta x),$$

where  $y_p$  is the Compton- $y$  measured in pixel  $p$ , and  $\Theta(x_p, x, \Delta x)$  is a binning operator for a bin centered at  $x$  with width  $\Delta x$ .

We then estimate the average  $y$  parameter in the  $x$ - $\psi$  plane for catalog  $c$  as  $\hat{y}_c(x, \psi) \equiv \sum_i s_y^i(x, \psi) / \sum_i s_N^i(x, \psi)$ .

3. We do this for the CMASS void catalog as well as the  $N_m = 1000$  mock catalogs, and finally estimate

<sup>3</sup> The Planck data is available at <http://irsa.ipac.caltech.edu/Missions/planck.html>.

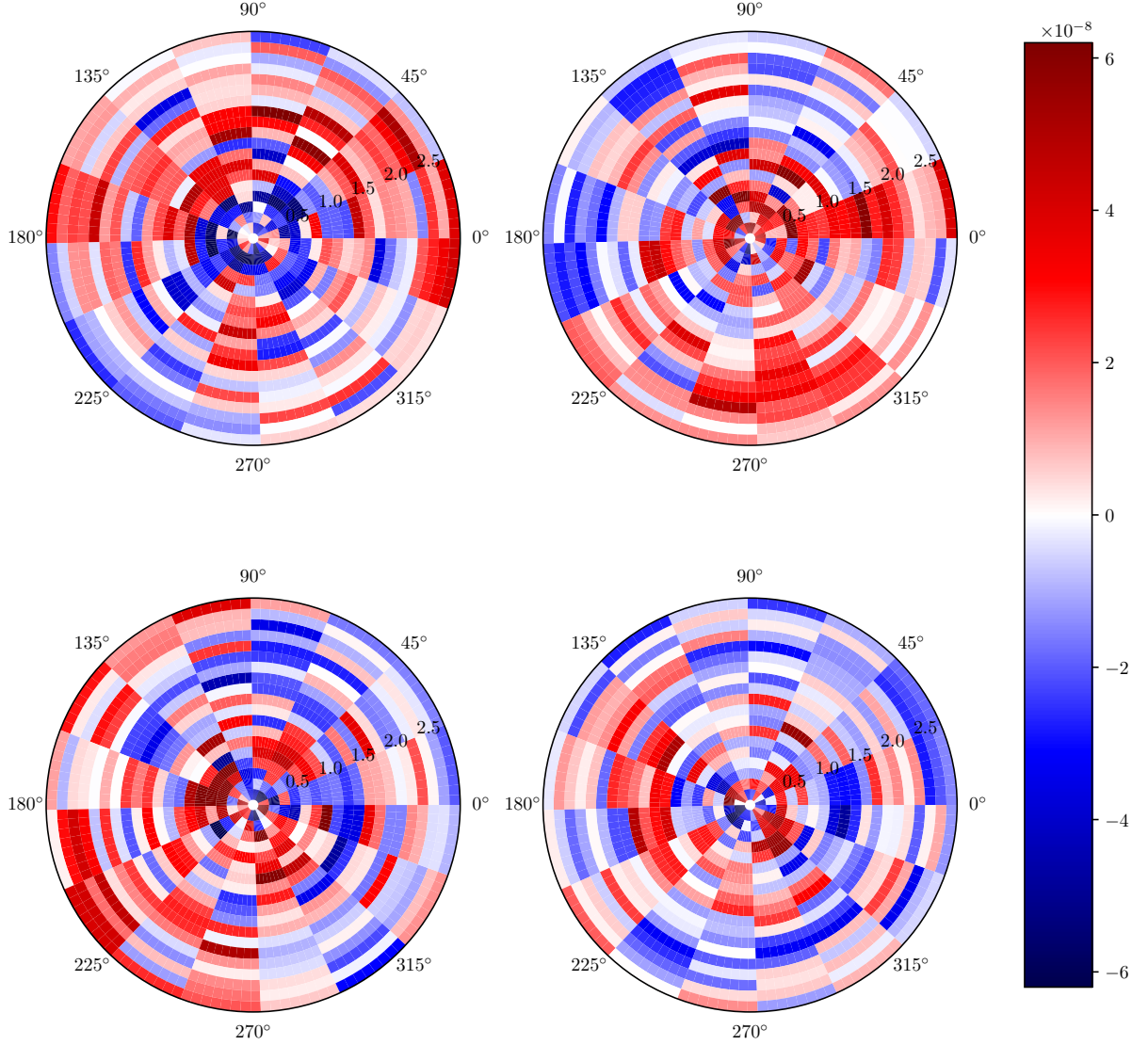


FIG. 1. 2-dimensional stacked tSZ signal in polar coordinates measured around the CMASS voids (top left) and three random mock void catalogues (top right and bottom). The data exhibits a noticeable average decrement below  $\theta \lesssim 0.7\theta_v$ , where  $\theta_v$  is the angle subtended by the void effective radius.

the average tSZ signal corrected for sky coverage and completeness by subtracting the mock average:

$$\bar{y}(x, \psi) = \hat{y}_{\text{CMASS}}(x, \psi) - \frac{1}{N_m} \sum_{c=1}^{N_m} \hat{y}_c(x, \psi). \quad (6)$$

In broad terms, the estimator is therefore a simple stack around voids of the  $y$  map in polar coordinates scaled by the effective void size. We have not implemented further refinements to the method, such as optimally filtering the  $y$  map for each void as done in e.g. [29], which might be able to marginally enhance the significance of this measurement, in order to facilitate the computation of the associated theoretical prediction. In our analysis we computed  $\bar{y}(\theta/\theta_v, \psi)$  in 20 radial bins for  $0 \leq \theta/\theta_v \leq 3$

and 16 angular bins for  $0 \leq \psi < 2\pi$ .

Figure 1 shows the stacked SZ signal around voids in polar coordinates for the CMASS catalog (upper left) and for three random mocks. Although the measurement is noisy, a decrement in  $y$  for  $x < 1$  with respect to the mean can clearly be appreciated in the real data.

Although the two-dimensional stacks are useful for visualization purposes, we do not expect a preferred orientation of the void signal, and therefore we proceed by considering only the radial tSZ profile (i.e. summing  $s_y$  and  $s_N$  over  $\psi$ ) as our data vector. We further limit the size of this vector to the 13  $x$ -bins with  $x < 24$ , and write the profile measured in the  $k$ -th bin as  $\bar{y}_k$ .



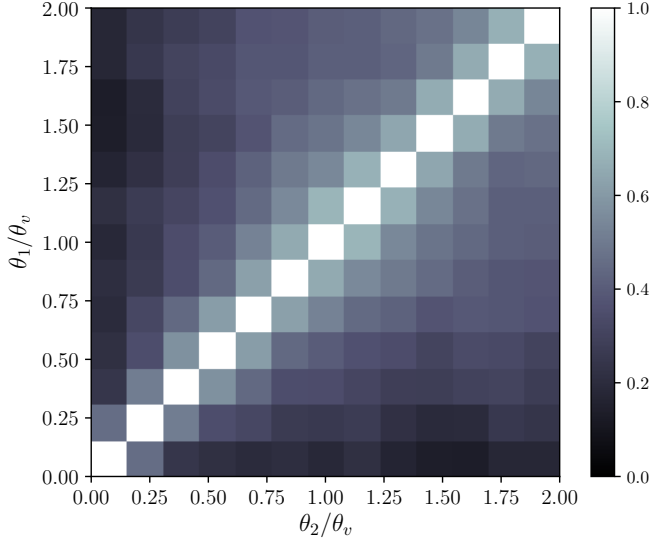


FIG. 2. Radial tSZ profile around voids estimated from the CMASS void catalog (red circles with error bars). The dashed black line corresponds to the theoretical expectation based on the model described in Section II, while the black solid line corresponds to the best-fit model found by scaling the fiducial prediction by an amplitude  $\alpha_v$ .

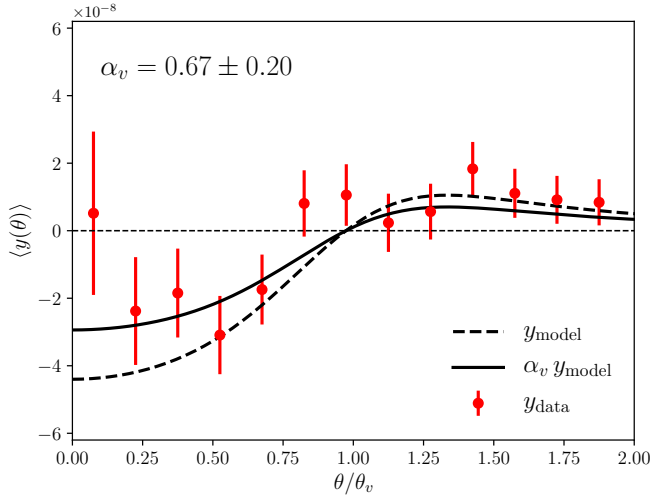


FIG. 3. Radial tSZ profile around voids estimated from the CMASS void catalog (red circles with error bars). The dashed black line corresponds to the theoretical expectation based on the model described in Section II, while the black solid line corresponds to the best-fit model found by scaling the fiducial prediction by an amplitude  $\alpha_v$ .

We estimated the covariance matrix of  $\bar{y}_k$  from the scatter of the 1000 mock catalogs:

$$C_{kk'} = \frac{1}{N_m} \sum_{c=1}^{N_m} (\bar{y}_k^c - \langle \bar{y}_k \rangle) (\bar{y}_{k'}^c - \langle \bar{y}_{k'} \rangle), \quad (7)$$

where  $\bar{y}_k^c$  is the measurement in the  $c$ -th mock, and  $\langle \bar{y} \rangle$  is the average across mocks. Figure 2 shows the estimated correlation matrix  $R_{kk'} \equiv C_{kk'}/\sqrt{C_{kk}C_{k'k'}}$ . Note that, because of the beam smoothing of the  $y$  maps, as well as the mixing of scales caused by the effective rescaling of the map with void size, there are significant off-diagonal contributions to the covariance, which need to be accounted for.

In order to quantify the significance of this measurement or the degree of agreement with a given model  $y_k^{\text{mod}}$ , we compute the  $\chi^2$ :

$$\chi^2(y^{\text{mod}}) \equiv \sum_{k,k'} (\bar{y}_k - y_k^{\text{mod}}) I_{kk'} (\bar{y}_{k'} - y_{k'}^{\text{mod}}), \quad (8)$$

where  $I_{kk'}$  is the inverse covariance matrix. We estimate  $I_{kk'}$  as the inverse of the sample covariance  $C_{kk'}$  corrected for the overall scaling factor prescribed by [30]:

$$I_{kk'} = \frac{N_m - n_d - 2}{N_m - 1} (C^{-1})_{kk'}, \quad (9)$$

where  $n_d$  is the size of the data vector. We verified that the distribution of  $\chi^2$  values for the 1000 mock void catalogues for a null model ( $y^{\text{mod}} = 0$ , since the mocks and  $y$  maps are uncorrelated) is well described by a “chi-squared” distribution with 13 degrees of freedom. Therefore, the  $\chi^2$  can be reliably interpreted as the likelihood of  $y^{\text{mod}}$  given the data  $\bar{y}_k$ .

As a model for the expected tSZ signal in voids we use the theoretical prediction described in Section II and scaled by an amplitude  $\alpha_v$  that we fit for. Since this is a linear model, the best-fit and standard deviation of  $\alpha_v$  can be computed analytically as:

$$\alpha_v = \frac{\sum_{k,k'} \bar{y}_k^{\text{mod}} I_{kk'} \bar{y}_{k'}}{\sum_{k,k'} \bar{y}_k^{\text{mod}} I_{kk'} \bar{y}_{k'}^{\text{mod}}}, \quad (10)$$

$$\sigma(\alpha_v) = \left[ \sum_{k,k'} \bar{y}_k^{\text{mod}} I_{kk'} \bar{y}_{k'}^{\text{mod}} \right]^{-1}, \quad (11)$$

where here  $y^{\text{mod}}$  is the theoretical model with a fiducial amplitude  $\alpha_v^{\text{fid}} = 1$ . Doing this we obtain a best-fit value and uncertainty  $\alpha_v = 0.668 \pm 0.199$ , corresponding to a  $\sim 3.4\sigma$  measurement of the tSZ signal in voids. Figure 3 shows the measured signal (red circles with error bars), the fiducial theory prediction (dashed black line) and the best-fit scaled model (solid black line). The  $\chi^2$  for this best-fit model is  $\chi^2(\alpha_v) = 15.3$ , corresponding to a probability-to-exceed (PTE) of 0.22 for 12 degrees of freedom. In contrast, for the null model we obtain  $\chi^2(\text{null}) = 26.6$ , with a PTE of 0.012. The significance of this measurement in terms of a  $\chi^2$ -difference is therefore  $\sqrt{\Delta\chi^2} = 3.36$ , in agreement with our previous estimate.

### C. Null tests and systematics

In order to test the robustness of this measurement, we have studied the possible impact of certain systematic un-

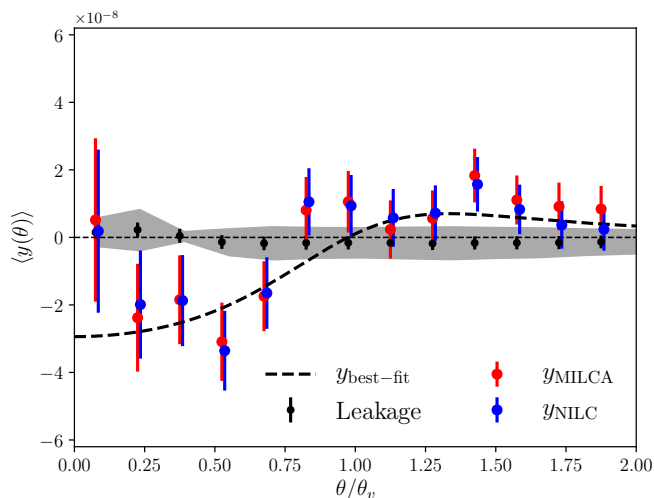


FIG. 4. Radial tSZ profile around voids estimated from the CMASS void catalog (red circles with error bars). The dashed black line corresponds to the theoretical expectation based on the model described in Section II, while the black solid line corresponds to the best-fit model found by scaling the fiducial prediction by an amplitude  $\alpha_v$ .

certainties and performed a number of consistency tests.

A first simple test for the presence of systematic errors is cross-correlating the CMASS voids with the “half-difference” Compton  $y$  map, constructed by differencing the  $y$  maps constructed using the first and second halves of stable pointing periods, and distributed together with the full MILCA map. The half-difference map should therefore contain only noise and no real  $y$  signal. We carried out the same analysis described in Section IV B on this half-difference map, including the computation of the associated covariance matrix, and find that the signal measured from the data is compatible with zero, with a  $\chi^2 = 12.8$  (PTE = 0.464).

We have also studied the consistency of our measurement by repeating it on the NILC Compton- $y$  map. We find that the measured void  $y$  profile agrees with the measurement from the MILCA map up to an overall additive offset. As mentioned in Section III B and pointed out by [18], the NILC map suffers from a higher large-scale noise power than the MILCA (see e.g. Fig. 5 of [15]). This large-scale contribution, as well as the overall amplitude of the void signal, are much smaller ( $\sim O(10^{-8})$ ) than the typical per-pixel noise ( $\sim O(10^{-6})$ ). Therefore any imperfection in the removal of the mean contribution to the correlation function estimator (i.e. the second term on the right hand side of Eq. 6), such as small deviations in the BOSS mock void catalogues from the true BOSS footprint, may give rise to an overall offset in the estimator. This is particularly relevant for the void stacks, given the larger angular scales involved, compared to the usual stacking analyses around groups or clusters.

To correct for this issue, we introduce an extra free

parameter in our model, corresponding to an overall additive amplitude  $\alpha_{\text{off}}$ , and fit for it jointly with the amplitude of the void profile  $\alpha_v$ . The measurement of the void  $y$  profile in the NILC map corrected for this offset is shown as blue dots in Fig. 4, which also shows the original MILCA measurement in red. This procedure yields a measurement of  $\alpha_v$  from the NILC map that is in agreement with our previous estimate,  $\alpha_v = 0.64 \pm 0.21$ , with a similar significance. The measured offset  $\alpha_{\text{off}} = (1.4 \pm 0.5) \times 10^{-8}$  is significant at the  $\sim 2.8\sigma$  level, and the overall fit is good, with a PTE = 0.21. It is also worth pointing out that, after repeating this analysis on the MILCA map, we find that the measured offset is compatible with 0 in this case, and that the recovered value of  $\alpha_v$  and its significance does not change significantly with respect to the fiducial analysis.

Finally, we quantify the level of contamination of our measurement by other potential correlated components. In particular we focus on the contribution from imperfectly cleaned dust and CIB emission, which is a known contaminant of the Planck  $y$  maps DA: cites. To do this, we follow the procedure described in [18] and [31], making use of the Planck 545 GHz map as a tracer of dust. We outline the method here, and we refer the reader to these papers for further details.

We start by assuming that the  $y$  map is contaminated by CIB and galactic emission, such that the observed map is

$$y_{\text{obs}} = y_{\text{true}} + \alpha_{\text{CIB}} T_{\text{CIB}} + \alpha_{\text{gal}} T_{\text{gal}}, \quad (12)$$

and that the 545 GHz map is dominated by precisely these components

$$T_{545} = T_{\text{CIB}} + T_{\text{gal}}. \quad (13)$$

We can then determine the leakage amplitudes  $\alpha_{\text{CIB}}$  and  $\alpha_{\text{gal}}$  by analyzing the auto-correlation of the 545 GHz map and its cross-correlation with the observed  $y$  map. This also requires the use of existing models for the CIB power spectrum and its true cross-correlation with the tSZ signal, for which we use the measurements of [32] and [33] respectively. After masking 80% of the sky we obtain  $\alpha_{\text{CIB}} = (2.3 \pm 6.6) \times 10^{-7} (\text{MJy/sr})^{-1}$  and  $\alpha_{\text{gal}} = (-0.8 \pm 1.9) \times 10^{-7} (\text{MJy/sr})^{-1}$ .

Since the galactic component should not correlate with the void distribution (unless regions of large galactic dust absorption could affect the void finding procedure), the most dangerous source of leakage would be the CIB component. The contribution of this source of contamination to the measured  $y$  void profile,  $\bar{y}_{545}$  can therefore be quantified by repeating the void stacking measurement on the 545 GHz map and scaling the resulting signal,  $\bar{T}_{545}$  with  $\alpha_{\text{CIB}}$ :  $\bar{y}_{545} = \alpha_{\text{CIB}} \bar{T}_{545}$ . The resulting estimated leakage is shown as black dots in Figure 4, with the shaded region corresponding to the level of leakage allowed by the  $1\sigma$  uncertainties on  $\alpha_{\text{CIB}}$ . DA: Discuss more. Say that this agrees with the rough expectation based on naive cross-correlation.

## V. DISCUSSION

Quisque ullamcorper placerat ipsum. Cras nibh. Morbi vel justo vitae lacus tincidunt ultrices. Lorem ipsum dolor sit amet, consectetur adipiscing elit. In hac habitasse platea dictumst. Integer tempus convallis augue. Etiam facilisis. Nunc elementum fermentum wisi. Aenean placerat. Ut imperdiet, enim sed gravida sollicitudin, felis odio placerat quam, ac pulvinar elit purus eget enim. Nunc vitae tortor. Proin tempus nibh sit amet nisl. Vivamus quis tortor vitae risus porta vehicula.

## ACKNOWLEDGEMENTS

The authors would like to thank Nick Battaglia, Adam Lidz and Mark Richardson for useful comments and discussions. DA also thanks the Center for Computational Astrophysics, part of the Simons Foundation, for their hospitality. DA acknowledges support from the Science and Technology Facilities Council and the Leverhulme and Beecroft Trusts. **DA: more?**

- 
- [1] R. A. Sunyaev and Y. B. Zeldovich, Comments on Astrophysics and Space Physics **4**, 173 (1972).
  - [2] E. Komatsu and U. Seljak, *MNRAS* **327**, 1353 (2001), [astro-ph/0106151](#).
  - [3] H. J. Mo and S. D. M. White, *MNRAS* **282**, 347 (1996), [astro-ph/9512127](#).
  - [4] P. Chang, A. E. Broderick, and C. Pfrommer, *Astrophys. J.* **752**, 23 (2012), [arXiv:1106.5504](#).
  - [5] J. S. Bolton, M. Viel, T.-S. Kim, M. G. Haehnelt, and R. F. Carswell, *MNRAS* **386**, 1131 (2008), [arXiv:0711.2064](#).
  - [6] S. Gottlöber, E. L. Lokas, A. Klypin, and Y. Hoffman, *MNRAS* **344**, 715 (2003), [astro-ph/0305393](#).
  - [7] D. M. Goldberg and M. S. Vogele, *Astrophys. J.* **605**, 1 (2004), [astro-ph/0307191](#).
  - [8] M. C. Martino and R. K. Sheth, *MNRAS* **394**, 2109 (2009), [arXiv:0901.0757 \[astro-ph.CO\]](#).
  - [9] D. Alonso, E. Eardley, and J. A. Peacock, *MNRAS* **447**, 2683 (2015), [arXiv:1406.4159](#).
  - [10] J. L. Tinker, B. E. Robertson, A. V. Kravtsov, A. Klypin, M. S. Warren, G. Yepes, and S. Gottlöber, *Astrophys. J.* **724**, 878 (2010), [arXiv:1001.3162](#).
  - [11] N. Battaglia, J. R. Bond, C. Pfrommer, and J. L. Sievers, *Astrophys. J.* **758**, 75 (2012), [arXiv:1109.3711](#).
  - [12] Q. Mao, A. A. Berlind, R. J. Scherrer, M. C. Neyrinck, R. Scoccimarro, J. L. Tinker, C. K. McBride, D. P. Schneider, K. Pan, D. Bizyaev, E. Malanushenko, and V. Malanushenko, *Astrophys. J.* **835**, 161 (2017), [arXiv:1602.02771](#).
  - [13] M. C. Neyrinck, *MNRAS* **386**, 2101 (2008), [arXiv:0712.3049](#).
  - [14] B. Reid, S. Ho, N. Padmanabhan, W. J. Percival, J. Tinker, R. Tojeiro, M. White, D. J. Eisenstein, C. Maraston, A. J. Ross, A. G. Sánchez, D. Schlegel, E. Sheldon, M. A. Strauss, D. Thomas, D. Wake, F. Beutler, D. Bizyaev, A. S. Bolton, J. R. Brownstein, C.-H. Chuang, K. Dawson, P. Harding, F.-S. Kitaura, A. Leauthaud, K. Masters, C. K. McBride, S. More, M. D. Olmstead, D. Oravetz, S. E. Nuza, K. Pan, J. Parejko, J. Pforr, F. Prada, S. Rodríguez-Torres, S. Salazar-Albornoz, L. Samushia, D. P. Schneider, C. G. Scóccola, A. Simmons, and M. Vargas-Magana, *MNRAS* **455**, 1553 (2016), [arXiv:1509.06529](#).
  - [15] Planck Collaboration, N. Aghanim, M. Arnaud, M. Ashdown, J. Aumont, C. Baccigalupi, A. J. Banday, R. B. Barreiro, J. G. Bartlett, N. Bartolo, and et al., *A&A* **594**, A22 (2016), [arXiv:1502.01596](#).
  - [16] G. Hurier, J. F. Macías-Pérez, and S. Hildebrandt, *A&A* **558**, A118 (2013), [arXiv:1007.1149 \[astro-ph.IM\]](#).
  - [17] M. Remazeilles, J. Delabrouille, and J.-F. Cardoso, *MNRAS* **410**, 2481 (2011), [arXiv:1006.5599](#).
  - [18] V. Vikram, A. Lidz, and B. Jain, *MNRAS* **467**, 2315 (2017), [arXiv:1608.04160](#).
  - [19] Planck Collaboration, P. A. R. Ade, N. Aghanim, M. Arnaud, M. Ashdown, J. Aumont, C. Baccigalupi, A. J. Banday, R. B. Barreiro, R. Barrena, and et al., *A&A* **594**, A27 (2016), [arXiv:1502.01598](#).
  - [20] Planck Collaboration, R. Adam, P. A. R. Ade, N. Aghanim, Y. Akrami, M. I. R. Alves, F. Argüeso, M. Arnaud, F. Arroja, M. Ashdown, and et al., *A&A* **594**, A1 (2016), [arXiv:1502.01582](#).
  - [21] S. Arbabi-Bidgoli and V. Müller, *MNRAS* **332**, 205 (2002), [astro-ph/0111581](#).
  - [22] E. Ricciardelli, V. Quilis, and J. Varela, *MNRAS* **440**, 601 (2014), [arXiv:1402.2976](#).
  - [23] S. Nadathur, S. Hotchkiss, J. M. Diego, I. T. Iliev, S. Gottlöber, W. A. Watson, and G. Yepes, in *The Zeldovich Universe: Genesis and Growth of the Cosmic Web*, IAU Symposium, Vol. 308, edited by R. van de Weygaert, S. Shandarin, E. Saar, and J. Einasto (2016) pp. 542–545, [arXiv:1412.8372](#).
  - [24] N. Hamaus, P. M. Sutter, and B. D. Wandelt, *Physical Review Letters* **112**, 251302 (2014), [arXiv:1403.5499](#).
  - [25] P. M. Sutter, G. Lavaux, N. Hamaus, B. D. Wandelt, D. H. Weinberg, and M. S. Warren, *MNRAS* **442**, 462 (2014), [arXiv:1309.5087](#).
  - [26] S. E. Nuza, A. G. Sánchez, F. Prada, A. Klypin, D. J. Schlegel, S. Gottlöber, A. D. Montero-Dorta, M. Manera, C. K. McBride, A. J. Ross, R. Angulo, M. Blanton, A. Bolton, G. Favole, L. Samushia, F. Montesano, W. J. Percival, N. Padmanabhan, M. Steinmetz, J. Tinker, R. Skibba, D. P. Schneider, H. Guo, I. Zehavi, Z. Zheng, D. Bizyaev, O. Malanushenko, V. Malanushenko, A. E. Oravetz, D. J. Oravetz, and A. C. Shelden, *MNRAS* **432**, 743 (2013), [arXiv:1202.6057](#).
  - [27] G. Pollina, N. Hamaus, K. Dolag, J. Weller, M. Baldi, and L. Moscardini, *MNRAS* **469**, 787 (2017), [arXiv:1610.06176](#).
  - [28] N. Hamaus, M.-C. Cousinou, A. Pisani, M. Aubert, S. Escoffier, and J. Weller, *JCAP* **7**, 014 (2017), [arXiv:1705.05328](#).

- [29] Y.-C. Cai, M. Neyrinck, Q. Mao, J. A. Peacock, I. Szapudi, and A. A. Berlind, *MNRAS* **466**, 3364 (2017), [arXiv:1609.00301](#).
- [30] J. Hartlap, P. Simon, and P. Schneider, *A&A* **464**, 399 (2007), [astro-ph/0608064](#).
- [31] J. C. Hill and D. N. Spergel, *JCAP* **2**, 030 (2014), [arXiv:1312.4525](#).
- [32] Planck Collaboration, P. A. R. Ade, N. Aghanim, C. Armitage-Caplan, M. Arnaud, M. Ashdown, F. Atrio-Barandela, J. Aumont, C. Baccigalupi, A. J. Banday, and et al., *A&A* **571**, A30 (2014), [arXiv:1309.0382](#).
- [33] Planck Collaboration, P. A. R. Ade, N. Aghanim, M. Arnaud, J. Aumont, C. Baccigalupi, A. J. Banday, and et al., *A&A* **594**, A23 (2016), [arXiv:1509.06555](#).
- [34] H. Bondi, *MNRAS* **107**, 410 (1947).

### Appendix A: The effective-universe approach to void-related quantities

It is a well-known result, valid in both Newtonian and relativistic gravitational theory (e.g. [34]), that a spherically-symmetric overdensity residing in an otherwise homogeneous Universe will evolve, at any distance  $r$  from its centre, as a parallel Friedmann-Lemaître-Robertson-Walker universe with effective cosmological parameters. These can be related to the density profile  $\delta(r)$  and local infall velocity of the overdensity (the latter defining the local expansion rate) as:

$$\Omega_M(r) = \Omega_M^{\text{BG}} \frac{1 + \Delta(r)}{\eta^2(r)}, \quad \Omega_\Lambda(r) = \frac{\Omega_\Lambda^{\text{BG}}}{\eta^2(r)}, \quad (\text{A1})$$

$$H_0(r) = H_0^{\text{BG}} \eta(r), \quad \Delta(r) \equiv \frac{3}{r^3} \int_0^r ds s^2 \delta(s), \quad (\text{A2})$$

where  $\Delta(r)$  is the average overdensity enclosed within a sphere of radius  $r$ , and all quantities labelled BG are the cosmological parameters of the background universe. The ratio between expansion rates can be fixed by imposing a homogeneous age of the Universe:

$$t_{\text{BB}} = \frac{1}{H_0} \int_0^1 \frac{dx}{x \sqrt{\Omega_M x^{-3} + \Omega_\Lambda + \Omega_K x^{-2}}}, \quad (\text{A3})$$

effectively making the perturbation a purely growing mode that vanishes at early times.

The computation of the background tSZ signal (Eq. 4) requires an estimate of the halo mass function, which depends on the evolution of both the background and linear perturbations. For deep underdensities, the cosmological constant's contribution to the total energy density dominates over that of matter, and therefore perturbations grow more slowly at late times than in the background cosmology. This effect can be taken into account by scaling the value of  $\sigma_8$  outside the void by the ratio of the linear growth factors in the effective and background cosmologies with the same normalization at early times.